Observation of Floquet bands in driven spin-orbit-coupled Fermi gases

Lianghui Huang,[1,2] Peng Peng,[1,2] Donghao Li,[1,2] Zengming Meng,[1,2] Liangchao Chen,[1,2] Chunlei Qu,[3,4,5] Pengjun Wang,[1,2,*] Chuanwei Zhang,[3,†] and Jing Zhang[1,6,‡]

[1]*State Key Laboratory of Quantum Optics and Quantum Optics Devices, Institute of Opto-Electronics, Shanxi University, Taiyuan 030006, People's Republic of China*
[2]*Collaborative Innovation Center of Extreme Optics, Shanxi University, Taiyuan 030006, People's Republic of China*
[3]*Department of Physics, The University of Texas at Dallas, Richardson, Texas 75080, USA*
[4]*INO-CNR BEC Center and Dipartimento di Fisica, Università di Trento, 38123 Povo, Italy*
[5]*JILA and Department of Physics, University of Colorado, Boulder, Colorado 80309, USA*
[6]*Synergetic Innovation Center of Quantum Information and Quantum Physics, University of Science and Technology of China, Hefei, Anhui 230026, People's Republic of China*

Periodic driving of a quantum system can significantly alter its energy bands and even change the band topology, opening a completely new avenue for engineering novel quantum matter. Although important progress has been made recently in measuring topological properties of Floquet bands in different systems, direct experimental measurement of full Floquet band dispersions and their topology change is still demanding. Here we directly measure Floquet band dispersions in a periodically driven spin-orbit-coupled ultracold Fermi gas using spin-injection radio-frequency spectroscopy. We observe that the Dirac point originating from two-dimensional spin-orbit coupling can be manipulated to emerge at the lowest or highest two dressed bands by fast modulating Raman laser frequencies, demonstrating topological change of Floquet bands. Our work will provide a powerful tool for understanding fundamental Floquet physics as well as engineering exotic topological quantum matter.

I. INTRODUCTION

Engineering energy-band dispersions plays a crucial role for designing quantum materials with novel functionalities. Besides traditional methods in solid state, periodic modulation of system parameters can significantly alter the band dispersions of a quantum matter such as turning a trivial insulator into a topological one [1–3]. Thanks to Floquet theory, such periodic-driven quantum systems can be described by an effective static Floquet Hamiltonian, which may exhibit distinct properties compared to their unmodulated counterparts. Experimentally, such Floquet band engineering has been recently investigated in atomic [4,5], photonic [6], and solid-state systems [7].

Ultracold atomic gases, due to their unprecedented tunability, provide an ideal platform for the investigation of Floquet physics [8]. As a prominent example, by loading ultracold atoms in a periodically modulated optical honeycomb lattice, a recent experiment [9] has realized the Haldane model that exhibits the anomalous quantum Hall effect [10]. So far, cold-atom experiments have mainly focused on detecting Floquet band structures and their properties indirectly, such as through atomic transport [9,11,12] along a path in momentum space, by adiabatically loading bosonic atoms to band minima [13–16] or by measuring the spin textures [17]. These experimental techniques may not work at band crossing points, which play a crucial role for determining band topology and its phase transition, and cannot be used to explore properties of every Floquet band, such as certain central static bands and all Floquet sidebands. Therefore, a direct measurement of the Floquet band dispersions, including the sidebands, in the full momentum space and the change of their topological properties is highly demanding in atomic systems.

Dirac points are topological band touching points with linear dispersions. In two dimension (2D), the topology of a Dirac point is characterized by the singularity of the Berry curvature at the point and nonzero Berry phase for a path enclosing the point in the momentum space. Therefore, Dirac-point creation and annihilation showcase one type of topological change of band dispersions of a quantum matter [18]. 2D spin-orbit coupling (SOC), such as Rashba SOC, naturally possesses a Dirac point in its band dispersion. It is well known that SOC plays a key role in many exotic topological materials [19,20]. In ultracold atoms, synthetic one-dimensional (1D) SOC (an equal sum of Rashba [21] and Dresselhaus [22] SOC) was first experimentally realized using a pair of counterpropagating Raman lasers to dress two atomic spin states [23–32]. Recently, by coupling three internal spin states of ultracold ^{40}K Fermi gases through three Raman lasers propagating in a plane, a 2D SOC characterized by the emergence of a Dirac point has been observed [33] (recently, 2D SOC was also realized using a lattice-based scheme [34]). Furthermore, an energy gap which is crucial for the investigation of topological physics in ultracold-atomic gases can be generated at the position of the Dirac point by tuning the polarization of the Raman lasers [35].

*pengjun_wang@sxu.edu.cn
†chuanwei.zhang@utdallas.edu
‡jzhang74@sxu.edu.cn; jzhang74@yahoo.com

In this article, we utilize 2D spin-orbit-coupled Fermi gases as a platform to investigate Floquet band engineering. By periodically modulating the detunings of two Raman lasers through their frequencies, we can manipulate the strength and even the sign of the Raman coupling of the effective Floquet Hamiltonian and therefore modify the position of the Dirac point in the Floquet band. For suitable modulations, the Dirac point initially located at the lower two dressed bands can disappear and then emerge at the upper two bands, indicating a topological change of the Floquet band structure. Using spin-injection radio-frequency (rf) spectroscopy, we directly measure the full Floquet band dispersions and observe their topology change induced by such modulations [36] in experiment. We find that the resulting Floquet bands and their topology change depend strongly on the relative phase between two modulations of two Raman laser detunings. Our results showcase the 2D spin-orbit-coupled Fermi gas as a powerful platform for exploring Floquet band engineering and exotic quantum matter [37–39].

The paper is structured as follows. In Sec. II, we present our experimental setup and methods. In Sec. III, we discuss the effective Hamiltonian of the driven system. Sections IV and V show the observed Floquet band dispersion and the role of the relative driving phase, respectively. Finally, Sec. VI includes our concluding remarks.

II. EXPERIMENTAL SETUP

The experimental setup for generating 2D SOC is the same as that in our previous experiment [33] (see also Appendices A and B). As shown in Fig. 1(a), three hyperfine spin states of the ^{40}K Fermi gas are coupled to the electronic excited states by three far-detuned Raman lasers, with the corresponding two-photon Raman coupling strengths between hyperfine states $|j\rangle$ and $|j'\rangle$ denoted by $\Omega_{jj'}$. The three Raman lasers propagate in the xy plane [Fig. 1(b)], and thus the motion of the atoms along the z direction is decoupled from the internal degrees of freedom. The two-photon Raman detunings are modulated as $\delta_2 = \delta_{2(0)} + \delta_m \cos(\omega t)$ and $\delta_3 = \delta_{3(0)} + \delta_m \cos(\omega t + \phi_0)$ by varying the frequencies of the Raman lasers 2 and 3. Here, $\delta_{2(0)}$ ($\delta_{3(0)}$) corresponds to the original two-photon Raman detuning between Raman lasers 1 and 2 (1 and 3) without the fast modulation (i.e., $\delta_{1(0)}$ is chosen as 0); ϕ_0 is the initial relative phase between two modulations, which could be tuned arbitrarily in experiment.

The three spin states are selected within the $4\,^2S_{1/2}$ ground electronic manifold with $|1\rangle = |F = 7/2, m_F = 1/2\rangle$, $|2\rangle = |9/2, 1/2\rangle$, and $|3\rangle = |9/2, 3/2\rangle$, where (F, m_F) are the quantum numbers for hyperfine spin states. The experiment starts with a Fermi gas of $N = 2 \times 10^6$ ^{40}K atoms in a crossed 1064 nm optical dipole trap at $T/T_F \approx 0.3$, where T_F is the Fermi temperature defined by $T_F = (6N)^{1/3}\hbar\bar{\omega}/k_B$ and $\bar{\omega} \simeq 2\pi \times 80$ Hz labels the geometric trapping frequency. The fermionic atoms are transferred into $|9/2, 5/2\rangle$ as the initial state via a rapid adiabatic passage induced by a rf field at 19.6 G. Then a homogeneous bias magnetic field along the z axis (gravity direction) is ramped to $B_0 = 121.4$ G by a pair of coils operating in the Helmholtz configuration, splitting the $|3\rangle$ and $|2\rangle$ Zeeman states by ~ 38.7 MHz and the $|1\rangle$ and $|2\rangle$ states by 1293 MHz. The large Zeeman splitting would isolate
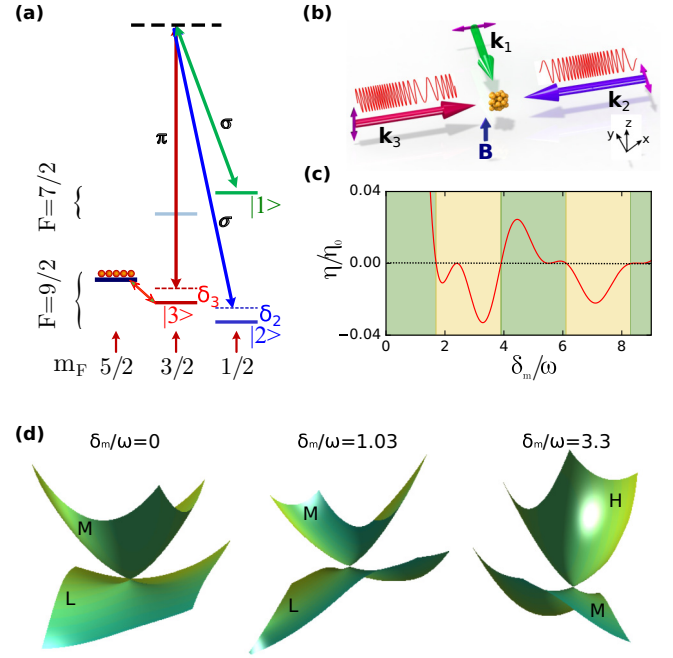
FIG. 1. (a) Energy-level diagram of Fermi gases ^{40}K. Three hyperfine spin states are coupled with the electronic excited states through three Raman lasers. The atoms are initially prepared in the free reservoir spin state $|9/2, 5/2\rangle$. (b) Configuration of three Raman lasers in the xy plane. The detunings of the Raman lasers 2 and 3 are modulated as $\delta_{2(0)} + \delta_m \cos(\omega t)$ and $\delta_{3(0)} + \delta_m \cos(\omega t + \phi_0)$. (c) Plot of the product of the effective Raman coupling strengths $\eta = \Omega'_{12}\Omega'_{13}\Omega'_{23}$ (scaled by $\eta_0 = \Omega_{12}\Omega_{13}\Omega_{23}$) as a function of the modulation parameter δ_m/ω. The background colors indicate the sign of η/η_0 which determines the position of the Dirac point. (d) Band structures near the Dirac points for different modulation parameter δ_m/ω. Only two bands that exhibit a Dirac point are shown, with the lower, middle, and higher bands labeled by L, M, and H, respectively. The relative phase $\phi_0 = \pi/2$ in (c) and (d).

these three hyperfine spin states from other ones in the Raman transitions. We choose the one-photon recoil momentum $\hbar k_r$ and the recoil energy $E_r = \hbar^2 k_r^2/2m = h \times 8.45$ kHz as the natural momentum and energy units. Here, $k_r = 2\pi/\lambda$ and λ is the wavelength of the Raman lasers. Using the acoustic-optic modulators (AOM), the frequencies of the Raman lasers 2 and 3 are modulated as $f_{2(0)} + \delta_{m2}\cos(\omega t)$ and $f_{3(0)} + \delta_{m3}\cos(\omega t + \phi_0)$, respectively, yielding the detuning modulations discussed above. The modulation frequency $\omega = 2\pi \times 100$ kHz is much larger than the other relevant energy scales.

III. EFFECTIVE HAMILTONIAN

The time-dependent Hamiltonian is given by (we have taken $E_r = \hbar^2 k_r^2/2m$ and $\hbar k_r$ as the units for the energy and momentum)

$$H = \begin{pmatrix} (\mathbf{k} - \mathbf{q}_1)^2 & -\frac{\Omega_{12}}{2} & -\frac{\Omega_{13}}{2} \\ -\frac{\Omega_{12}}{2} & (\mathbf{k} - \mathbf{q}_2)^2 + \delta_2 & -\frac{\Omega_{23}}{2} \\ -\frac{\Omega_{13}}{2} & -\frac{\Omega_{23}}{2} & (\mathbf{k} - \mathbf{q}_3)^2 + \delta_3 \end{pmatrix}. \quad (1)$$

Here, $\hbar \mathbf{k} = (\hbar k_x, \hbar k_y)$ denotes the momentum of atoms projected on the xy plane. The wave vectors are of three lasers $\mathbf{q}_1 = -k_r \hat{e}_y$, $\mathbf{q}_2 = -k_r \hat{e}_x$, and $\mathbf{q}_3 = k_r \hat{e}_x$.

The two time-varying detunings are modulated in the following way:

$$\delta_2 = \delta_{2(0)} + \delta_{m2} \cos(\omega t + \alpha), \tag{2}$$

$$\delta_3 = \delta_{3(0)} + \delta_{m3} \cos(\omega t + \alpha + \phi_0), \tag{3}$$

$$\tilde{H} = \begin{pmatrix} (\mathbf{k} - \mathbf{q}_1)^2 & -\frac{\Omega_{12}}{2} e^{-i\frac{\delta_{m2}}{\omega}\sin(\omega t + \alpha)} & -\frac{\Omega_{13}}{2} e^{-i\frac{\delta_{m3}}{\omega}\sin(\omega t + \alpha + \phi_0)} \\ -\frac{\Omega_{12}}{2} e^{i\frac{\delta_{m2}}{\omega}\sin(\omega t + \alpha)} & (\mathbf{k} - \mathbf{q}_2)^2 + \delta_{2(0)} & -\frac{\Omega_{23}}{2} e^{i\frac{\delta_{m2}}{\omega}\sin(\omega t + \alpha)} e^{-i\frac{\delta_{m3}}{\omega}\sin(\omega t + \alpha + \phi_0)} \\ -\frac{\Omega_{13}}{2} e^{i\frac{\delta_{m3}}{\omega}\sin(\omega t + \alpha + \phi_0)} & -\frac{\Omega_{23}}{2} e^{-i\frac{\delta_{m2}}{\omega}\sin(\omega t + \alpha)} e^{i\frac{\delta_{m3}}{\omega}\sin(\omega t + \alpha + \phi_0)} & (\mathbf{k} - \mathbf{q}_3)^2 + \delta_{3(0)} \end{pmatrix}.$$

The effective Hamiltonian is defined as the time average of $\tilde{H}$ over one driving period,

$$H_{\mathrm{eff}} = \frac{\omega}{2\pi} \int_0^{2\pi/\omega} \tilde{H}(t) dt$$

$$= \begin{pmatrix} (\mathbf{k} - \mathbf{q}_1)^2 & -\frac{\Omega'_{12}}{2} & -\frac{\Omega'_{13}}{2} \\ -\frac{\Omega'_{12}}{2} & (\mathbf{k} - \mathbf{q}_2)^2 + \delta_{2(0)} & -\frac{\Omega'_{23}}{2} \\ -\frac{\Omega'_{13}}{2} & -\frac{\Omega'_{23}}{2} & (\mathbf{k} - \mathbf{q}_3)^2 + \delta_{3(0)} \end{pmatrix}. \tag{4}$$

Therefore, the diagonal parts of the transformed Hamiltonian do not change while the nondiagonal parts will be averaged out, yielding static effective Raman couplings,

$$\Omega'_{12} = \Omega_{12} J_0\left(\frac{\delta_{m2}}{\omega}\right), \tag{5}$$

$$\Omega'_{13} = \Omega_{13} J_0\left(\frac{\delta_{m3}}{\omega}\right), \tag{6}$$

$$\Omega'_{23} = \Omega_{23}\left[J_0\left(\frac{\delta_{m2}}{\omega}\right) J_0\left(\frac{\delta_{m3}}{\omega}\right) + 2\sum_{n=1}^{\infty} J_n\left(\frac{\delta_{m2}}{\omega}\right) \times J_n\left(\frac{\delta_{m3}}{\omega}\right) \cos(n\phi_0)\right]. \tag{7}$$

Here, $J_n(x)$ is the nth-order Bessel function.

If $\delta_{m2} = \delta_{m3} \equiv \delta_m$, then Ω'_{23} can be simplified to

$$\Omega'_{23} = \Omega_{23} J_0\left[\frac{2\delta_m}{\omega}\sin(\phi_0/2)\right]. \tag{8}$$

Particularly, we find (i) $\Omega'_{23} = \Omega_{23}$ for $\phi_0 = 0$, (ii) $\Omega'_{23} = \Omega_{23} J_0(\sqrt{2}\delta_m/\omega)$ for $\phi_0 = \pi/2$, and (iii) $\Omega'_{23} = \Omega_{23} J_0(2\delta_m/\omega)$ for $\phi_0 = \pi$.

The effective Hamiltonian can also be derived based on a different approach introduced in Ref. [39]. The equation is

$$H_{\mathrm{eff}} = H_0 + \frac{1}{\omega}\sum_{j=1}^{\infty}\frac{1}{j}[V^{(j)}, V^{(-j)}]$$

$$+ \frac{1}{2\omega^2}\sum_j^{\infty}\frac{1}{j^2}([[V^{(j)}, H_0], V^{(-j)}] + \mathrm{H.c.}) + O\left(\frac{1}{\omega^3}\right), \tag{9}$$

where α is the unknown initial phase of the modulation and ϕ_0 is the relative phase between the two modulations.

To eliminate the time dependence of the original Hamiltonian, one can apply a time-dependent unitary transformation of the following form: $U = \mathrm{diag}(1, e^{-i\frac{\delta_{m2}}{\omega}\sin(\omega t + \alpha)}, e^{-i\frac{\delta_{m3}}{\omega}\sin(\omega t + \alpha + \phi_0)})$. The wave function is then transformed as $\tilde{\Psi} = U^{-1}\Psi$, while the Hamiltonian is transformed as $\tilde{H} = U^{-1}HU - iU^{-1}\frac{\partial U}{\partial t}$, i.e.,

where H_0 is the time-independent part of the original Hamiltonian and

$$V^{(\pm 1)} = \begin{pmatrix} 0 & 0 & 0 \\ 0 & \frac{\delta_{m2}}{2}e^{\pm i\alpha} & 0 \\ 0 & 0 & \frac{\delta_{m3}}{2}e^{\pm i(\alpha + \phi_0)} \end{pmatrix} \tag{10}$$

are the positive and negative frequency parts of the periodic driving of δ_2 and δ_3. This method becomes cumbersome for high-order terms. But for a high driving frequency limit, we can safely keep the first several terms and find the approximate effective Hamiltonian with good precision. Using the series expansions for Bessel functions, it is easy to find that the expression of the effective Raman coupling is the same (up to the order of $1/\omega^2$) as those derived in the previous method.

The effective 3×3 static Floquet Hamiltonian has three dressed bands, and the position of the Dirac point is determined by the sign of the quantity η/η_0 where $\eta = \Omega'_{12}\Omega'_{13}\Omega'_{23}$ and $\eta_0 = \Omega_{12}\Omega_{13}\Omega_{23}$. The Dirac point emerges at the crossing of the lower (upper) two bands for negative (positive) η [33]. By varying the modulating amplitude δ_m and relative phase ϕ_0, we can manipulate η [see Fig. 1(c)] and thus alter the topology of the Floquet band structure [Fig. 1(d)]. For the measurement, we use momentum-resolved spin-injection rf spectroscopy to study the energy-momentum dispersions of the dressed states, in which the atoms are driven from a free spin-polarized state (initial state) into the SOC dressed ones (final states).

IV. TOPOLOGY CHANGE OF FLOQUET BAND DISPERSIONS

The wavelengths of the Raman lasers are tuned to 768.85 nm between the D_1 line and D_2 line, making $\mathrm{sgn}(\eta/\eta_0) = -1$ for the Raman coupling strengths in the absence of the modulation $\delta_m = 0$. Therefore, the two lower-energy bands touch at a Dirac point which is observed in experiment, as shown in Fig. 2(a), with the three band dispersions measured by spin-injection rf spectroscopy. The band dispersions are also determined theoretically by calculating the eigenenergy spectrum of the effective static Floquet Hamiltonian and compared with the experimental results. The Berry curvature diverges at the Dirac point as a δ function, and the Berry phase is $\pm\pi$ along a closed
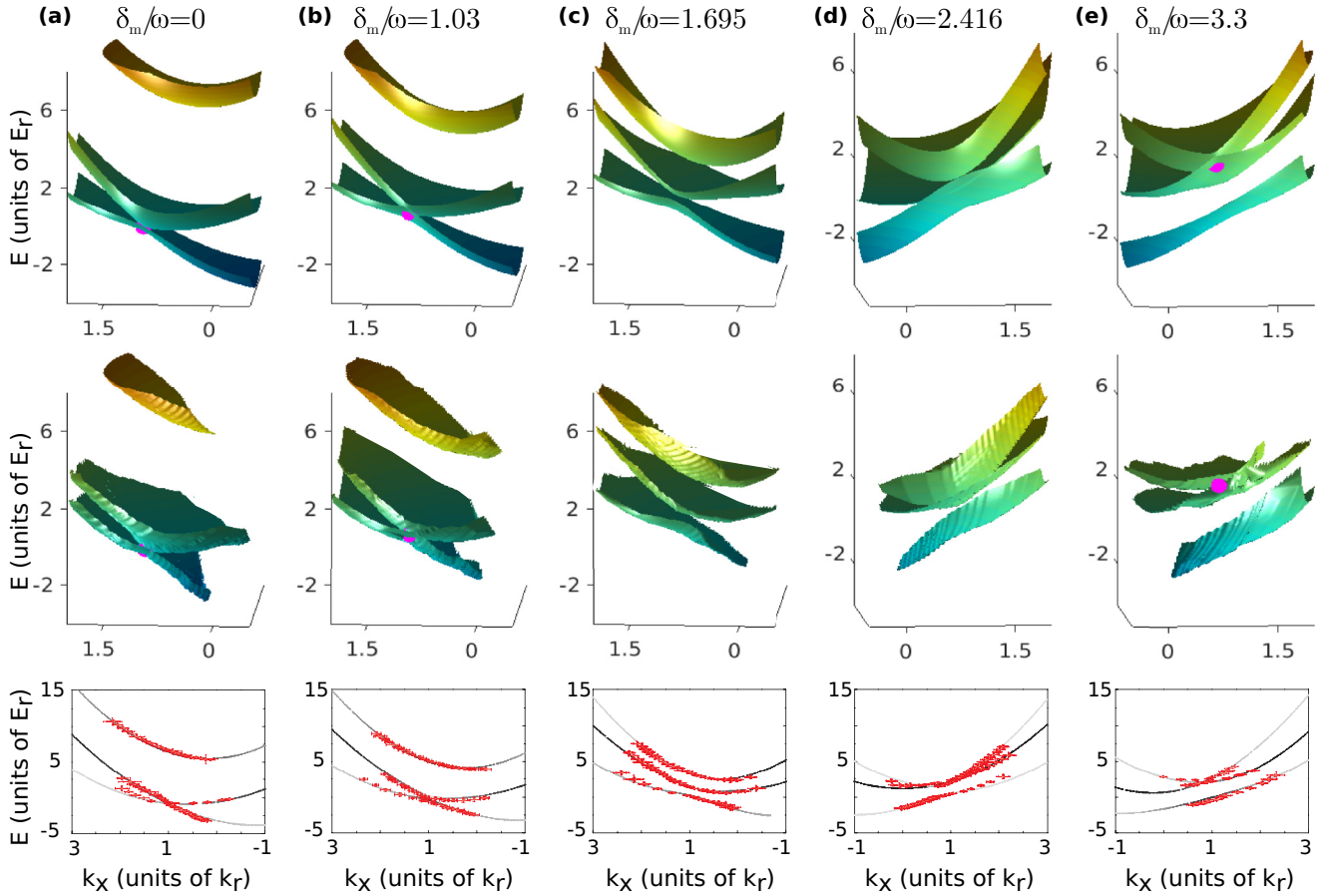
FIG. 2. Observation of Floquet band topological change. The upper and middle panels represent theoretically calculated and experimentally measured 2D Floquet band dispersions, respectively. The red dots represent the Dirac points. The lower panel represents corresponding 1D dispersions along (a)–(d) $k_y = 0.05k_r$ and (e) $k_y = -0.7k_r$, where the grayness of the lines indicates the population of the final state $|3\rangle$. The modulation amplitudes of the Raman detunings are (a) $\delta_m/\omega = 0$, (b) 1.03, (c) 1.695, (d) 2.416, and (e) 3.3. Other parameters are $\Omega_{12} = 5.46E_r$, $\Omega_{13} = 4.62E_r$, $\Omega_{23} = -4.2E_r$, $\delta_{2(0)} = -2.47E_r$, and $\delta_{3(0)} = 0.93E_r$. The relative phase is $\phi_0 = \pi/2$. Note that the orientation of the k_x axes is different for a better view of the band structures.

loop around the Dirac point; therefore, the lower two bands are topological, while the upper band is nontopological.

The role of the relative phase ϕ_0 will be examined in the last section. Without loss of generality in demonstrating the band topology change, we first consider the periodic modulations with the relative phase $\phi_0 = \pi/2$. By increasing δ_m/ω, the three effective Raman coupling strengths decrease, and the Dirac point moves in the momentum space, but still within the lowest two bands for a small δ_m/ω [see Fig. 2(b)]. When $\delta_m/\omega \approx 1.7$, $J_0(\sqrt{2}\delta_m/\omega) = 0$ and thus $\Omega'_{23} = 0$. The two spin states $|2\rangle$ and $|3\rangle$ decouple and the Dirac point moves to infinity, showing three Floquet bands which are gapped everywhere [see Fig. 2(c)]. When δ_m/ω is slightly larger than 1.7, the Dirac point reappears at the crossing of the two upper bands because Ω'_{23} changes sign and becomes positive. When $\delta_m/\omega \approx 2.4$, $J_0(\delta_m/\omega) = 0$ and thus $\Omega'_{12} = \Omega'_{13} = 0$, the two spin states $|2\rangle$ and $|3\rangle$ are coupled by an effective 1D SOC which does not exhibit a Dirac point. For our experimental parameters, the uncoupled free-particle dispersion band for spin state $|1\rangle$ intersects with the upper branch of the 1D SOC [Fig. 2(d)], where a small gap between these two dispersions is opened due to the finite driving frequency ω. By further increasing

δ_m/ω, Ω'_{12} and Ω'_{13} change sign simultaneously and thus the Dirac point remains at the same crossing as of the two upper dressed bands [see Fig. 2(e)]. Now the upper band initially without topological properties becomes topological and the lower band becomes nontopological.

We denote $\mathbf{k}_0 = (k_x^0, k_y^0)$ as the original position of the Dirac point in momentum space in the absence of modulation. In the presence of modulation, the position of the Dirac point is shifted to a different place and there is an energy separation at $\mathbf{k}_0$ between the two crossed bands. We characterize the three band dispersions by measuring the energy separations between the three dressed bands at the position of $\mathbf{k}_0$. In Fig. 3(a), we plot these energy separations as a function of the modulation parameter δ_m/ω. With the increase of δ_m/ω, the three effective Raman coupling strengths are decreased, the energy separation between the lower two bands at $\mathbf{k}_0$ is increased [blue line in Fig. 3(a)], while the separation between the upper two bands is decreased [red line in Fig. 3(a)]. The good agreement between experiment and theory demonstrates the expected modulation of the Floquet band dispersion.

In the presence of modulation, the current position of the Dirac point $\mathbf{k} = (k_x, k_y)$ is different from $\mathbf{k}_0$. For different values
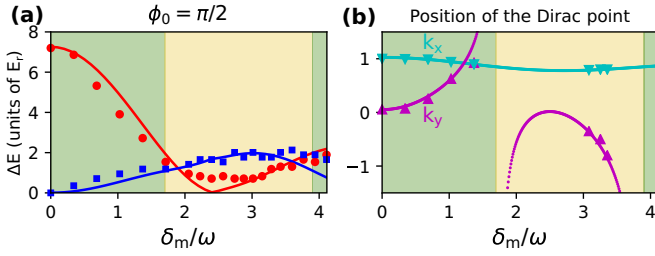
FIG. 3. (a) Energy separations between three energy bands at $\mathbf{k}_0$, i.e., the position of the Dirac point in the absence of modulation. The symbols and solid lines correspond to experimental and theoretical results, respectively. (b) Change of the position of the Dirac point as a function of the modulation parameter δ_m/ω. The magenta and cyan lines correspond to a theoretical plot of k_x and k_y of the Dirac point. The symbols correspond to the positions of the experimentally measured Dirac points. All other parameters are the same as Fig. 2. The background colors in both panels indicate whether the Dirac point exhibits at the crossing of the two lower (green) or the two higher (yellow) bands.

FIG. 4. Effect of the initial relative phase ϕ_0. The format and parameters are the same as Fig. 3, except that (a),(b) $\phi_0 = 0$ and (c),(d) $\phi_0 = \pi$, respectively. For $\phi_0 = 0$, the Raman coupling Ω_{23} is not modulated and the Dirac point remains at the crossing of two lower bands.

of δ_m/ω, it can be computed theoretically from the effective static Floquet Hamiltonian (4). In Fig. 3(b), we show the trajectory of the current Dirac point as a function of the modulation parameter δ_m/ω, together with the experimental measured positions for three values of δ_m/ω shown in Fig. 2. Across the points $\delta_m/\omega = z_{n,0}/\sqrt{2} = 1.7, 3.9, 6.1, 8.3, \ldots$, the Dirac point moves to infinity [Fig. 2(c)] and then reappears at the crossing of the other two dressed bands [Fig. 2(e)]. Here, $z_{n,0}$ are the zeros of the Bessel function, $J_0(z_{n,0}) = 0$. On the contrary, at the two sides of $\delta_m/\omega = 2.4, 5.5, 8.65, 11.8, \ldots$, two of the effective Raman couplings change sign simultaneously and the position of the Dirac point does not change. Such observed move of the topological Dirac point between the lower and upper two bands with increasing δ_m/ω showcases the topology change of the Floquet band structure of driven Fermi gases.

Before concluding this section, we remark that periodic driving not only modifies the band structure drastically, but also induces Floquet sidebands. The modulated Fermi gas provides an ideal platform to map out the sidebands using spin-injection rf spectroscopy. In our experiment, we are able to detect the lowest-order sidebands which are separated from the central bands by the driving frequency $\hbar\omega = h \times 100$ kHz. The characterization and understanding of the rf spectroscopy signal for the sidebands is left for further investigation.

V. EFFECT OF RELATIVE PHASE

In the presence of multiple modulations of the system parameters, the relative phase between these modulations plays a key role in the driven dynamics and the energy dispersions of the corresponding effective Hamiltonian are usually very different. A prominent example is the comparison between the circular and linear drivings of two components of a gauge field, where the former one breaks the time-reversal symmetry and may lead to the appearance of fascinating topological states while the latter one does not [7,9]. Here the relative phase ϕ_0 between the modulation of the two detunings can dramatically change, $\Omega_{23}' = J_0[2\delta_m \sin(\phi_0/2)/\omega]$ and thus affect the sign of
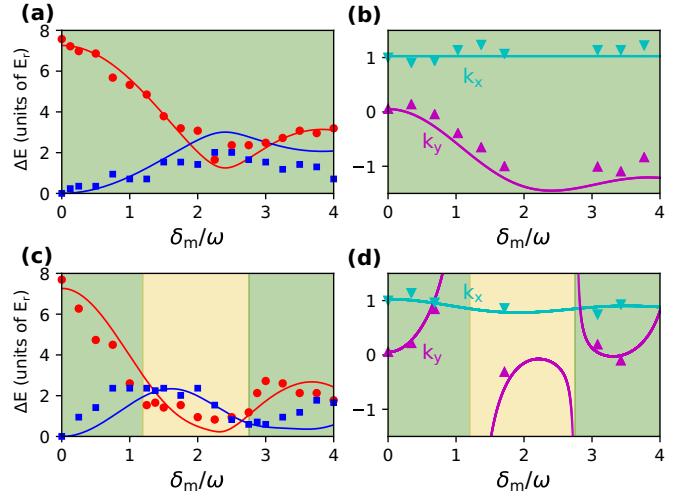
η/η_0 and the position of the Dirac point. In Figs. 4(a) and 4(c), we plot the band separations at the original Dirac point $\mathbf{k}_0$, similar to Fig. 3(a), but with $\phi_0 = 0$ and $\phi_0 = \pi$, respectively. The corresponding Dirac-point positions are shown in Figs. 4(b) and 4(d). When $\phi_0 = 0$, the Raman coupling Ω_{23}' does not change sign during the modulation. The simultaneous change of the other two Raman coupling strengths does not reverse the sign of the parameter η/η_0, and therefore the Dirac point always exhibits at the lower two bands [Fig. 4(b)]. However, similar to the case of $\phi_0 = \pi/2$, η/η_0 changes sign for $\phi_0 = \pi$, and thus the Dirac point moves from the lower two bands to the upper two bands and vice versa [Fig. 4(d)] with increasing modulation amplitude δ_m/ω.

VI. DISCUSSION

The motion of atoms along the z direction is decoupled from that in the xy plane; therefore the rf spectroscopy only detects the band dispersion in the xy plane although the Fermi gas can be 3D. For a 2D (or a fixed k_z plane in 3D) Fermi gas, a topological band gap at the Dirac point can be opened by varying the polarizations of the Raman lasers, which induces an imaginary part for the Raman coupling strength that corresponds to an effective perpendicular Zeeman field. For example, in a recent experiment [35], an imaginary term $i\Gamma$ was generated for the Raman coupling Ω_{12}. The exhibited energy gap Δ at the position of the original Dirac point is found to be proportional to Γ and the Chern number of the two bands is given by $\pm\text{sgn}(\Gamma\Omega_{13}\Omega_{23})$ [40]. In the presence of the same modulations that we explored, the real and imaginary parts of the Raman coupling Ω_{12} change sign simultaneously. Consequently, the Chern number of the two gapped bands are given by $\pm\text{sgn}(\eta/\eta_0)$ [$\mp\text{sgn}(\eta/\eta_0)$] if Γ is of the same (opposite) sign with Ω_{12} before the modulations are applied. This provides a useful guide to detect the topological properties of the driven energy bands in the presence of an energy gap.

Such topological band gaps support the existence of exotic Majorana fermions in 2D and Weyl fermions in 3D in the presence of pairing interactions, while the periodic driving provides a knob to tune topological band regions, yielding Floquet Majorana or Weyl fermions.

In conclusion, we have directly observed the topology change of the full Floquet band structure in a periodically driven quantum system using spin-injection rf spectroscopy. Our model system, i.e., periodically driven Fermi gases with 2D SOC, provides an ideal platform for testing and understanding rich Floquet physics and band engineering exotic quantum materials, as well as exploring interesting many-body and few-body interacting physics in Floquet systems.

FIG. 5. Schematic of generating the Raman lasers. $\lambda/2$: half-wave plate; $\lambda/4$: quarter-wave plate; PBS: polarized beam splitter; AOM: acousto-optic modulator.

APPENDIX A: SPIN-INJECTION SPECTROSCOPY

The Raman lasers are derived from a continuous-wave Ti-sapphire single-frequency laser with the wavelength $\lambda = 768.85$ nm, which are ramped up linearly from zero to their final intensity in 60 ms. Subsequently, a Gaussian-shape pulse with 450 μs of the rf field is applied to drive atoms from $|9/2, 5/2\rangle$ to the final empty SOC state. Since the spin state $|9/2, 5/2\rangle$ is coupled to the state $|3\rangle$ via rf, spin-injection rf spectroscopy will measure the weight of the $|3\rangle$ state and obtain the energy dispersions with 2D SOC. At last, the Raman lasers, the optical trap, and the magnetic field are switched off abruptly, and atoms freely expand for 12 ms in a magnetic-field gradient applied along the x axis. Absorption images are taken along the z direction. By counting the number of atoms in state $|3\rangle$ as a function of the momentum and the rf frequency from the absorption image, the energy-band structure and the position of the Dirac point can be determined.

APPENDIX B: THE CONFIGURATION OF RAMAN LASERS

The Raman lasers are derived from a continuous-wave Ti-sapphire single-frequency laser (M Squared lasers, SolsTiS) with the wavelength 768.85 nm, as shown in Fig. 5. The Raman laser 1 is sent through the two double-pass acousto-optic modulators (AOM) (3200-124, Crystal Technology, Inc) driven by two signal generators (N9310A, Agilent) and frequency shifted -212.975×4 MHz. The Raman lasers 2 and 3 double pass through two AOM and are frequency shifted $+201.144 \times 2$ and $+220.531 \times 2$ MHz, respectively. In order to periodically drive the two-photon Raman detuning, the Raman lasers 2 and 3 are frequency modulated, respectively, with $f_{2(0)} + \delta_{m2} \cos(\omega t)$ and $f_{3(0)} + \delta_{m3} \cos(\omega t + \phi_0)$, in which a signal generator (AFG3252 Textronix) generates $\cos(\omega t)$ and $\cos(\omega t + \phi_0)$ signal outputs simultaneously to externally modulate the frequencies of two signal generators (N5183A, Agilent) for Raman lasers 2 and 3. The modulation frequency response of the frequency modulation of the signal generator (N5183A, Agilent) may reach 3 MHz and the maximum deviation is about 10 MHz, which can satisfy the experimental requirement.

[1] T. Oka and H. Aoki, Photovoltaic Hall effect in graphene, Phys. Rev. B **79**, 081406(R) (2009).

[2] T. Kitagawa, E. Berg, M. Rudner, and E. Demler, Topological characterization of periodically driven quantums systems, Phys. Rev. B **82**, 235114 (2010).

[3] N. H. Linder, G. Refael, and V. Galitski, Floquet topological insulator in semiconductor quantum wells, Nat. Phys. **7**, 490 (2011).

[4] M. Aidelsburger, M. Atala, M. Lohse, J. T. Barreiro, B. Paredes, and I. Bloch, Realization of the Hofstadter Hamiltonian with Ultracold Atoms in Optical Lattices, Phys. Rev. Lett. **111**, 185301 (2013).

[5] H. Miyake, G. A. Siviloglou, C. J. Kennedy, W. C. Burton, and W. Ketterle, Realizing the Harper Hamiltonian with Laser-Assisted Tunneling in Optical Lattices, Phys. Rev. Lett. **111**, 185302 (2013).

[6] M. C. Rechtsman, J. M. Zeuner, Y. Plotnik, Y. Lumer, D. Podolsky, F. Dreisow, S. Nolte, M. Segev, and A. Szameit, Photonic Floquet topological insulators, Nature (London) **496**, 196 (2013).

[7] Y. H. Wang, H. Steinberg, P. Jarillo-Herrero, and N. Gedik, Observation of Floquet-Bloch states on the surface of a topological insulator, Science **342**, 453 (2013).

[8] A. Eckard, Colloquium: Atomic quantum gases in periodically driven optical lattices, Rev. Mod. Phys. **89**, 011004 (2017).

[9] G. Jotzu, M. Messer, R. Desbuquois, M. Lebrat, T. Uehlinger, D. Greif, and T. Esslinger, Experimental realization of the topological Haldane model with ultracold fermions, Nature (London) **515**, 237 (2014).

[10] F. D. M. Haldane, Model for a Quantum Hall Effect without Landau Levels: Condensed-Matter Realization of the "Parity Anomaly", Phys. Rev. Lett. **61**, 2015 (1988).

[11] M. Aidelsburger, M. Lohse, C. Schweizer, M. Atala, J. T. Barreiro, S. Nascimbène, N. R. Cooper, I. Bloch, and N. Goldman, Measuring the Chern number of Hofstadter bands with ultracold bosonic atoms, Nat. Phys. **11**, 162 (2015).

[12] M. Ölschläger, G. Wirth, T. Kock, and A. Hemmerich, Topologically Induced Avoided Band Crossing in an Optical Checkerboard Lattice, Phys. Rev. Lett. **108**, 075302 (2012).

[13] C. V. Parker, L.-C. Ha, and C. Chin, Direct observation of effective ferromagnetic domains of cold atoms in a shaken optical lattice, Nat. Phys. **9**, 769 (2013).

[14] K. Jiménez-Garzia, L. J. LeBlanc, R. A. Williams, M. C. Beeler, C. Qu, M. Gong, C. Zhang, and I. B. Spielman, Tunable Spin-Orbit Coupling via Strong Driving in Ultracold-Atom Systems, Phys. Rev. Lett. **114**, 125301 (2015).

[15] M. A. Khamehchi, C. Qu, M. E. Mossman, C. Zhang, and P. Engels, Spin-momentum coupled Bose-Einstein condensates with lattice band pseudospins, Nat. Commun. **7**, 10867 (2016).

[16] C. J. Kennedy, C. J. W. C. Burton, W. C. Chung, and W. Ketterle, Observation of Bose–Einstein condensation in a strong synthetic magnetic field, Nat. Phys. **11**, 859 (2015).

[17] M. Tarnowski, M. Nuske, N. Fläschner, B. Rem, D. Vogel, L. Freystatzky, K. Sengstock, L. Mathey, and C. Weitenberg, Observation of Topological Bloch-State Defects and Their Merging Transition, Phys. Rev. Lett. **118**, 240403 (2017).

[18] L. Tarruell, D. Greif, T. Uehlinger, G. Jotzu, and T. Esslinger, Creating, moving and merging Dirac points with a Fermi gas in a tunable honeycomb lattice, Nature (London) **483**, 302 (2012).

[19] M. Z. Hasan and C. L. Kane, Colloquium: Topological insulators, Rev. Mod. Phys. **82**, 3045 (2010).

[20] X.-L. Qi and S.-C. Zhang, Topological insulators and superconductors, Rev. Mod. Phys. **83**, 1057 (2011).

[21] Y. A. Bychkov and E. I. Rashba, Oscillatory effects and the magnetic susceptibility of carriers in inversion layers, J. Phys. C **17**, 6039 (1984).

[22] G. Dresselhaus, Spin-orbit coupling effects in zinc blende structures, Phys. Rev. **100**, 580 (1955).

[23] Y.-J. Lin, K. Jiménez-García, and I. B. Spielman, Spin-orbit-coupled Bose-Einstein condensates, Nature (London) **471**, 83 (2011).

[24] Z. Fu, P. Wang, S. Chai, L. Huang, and J. Zhang, Bose-Einstein condensate in a light-induced vector gauge potential using the 1064 nm optical dipole trap lasers, Phys. Rev. A **84**, 043609 (2011).

[25] J.-Y. Zhang *et al.*, Collective Dipole Oscillations of a Spin-Orbit Coupled Bose-Einstein Condensate, Phys. Rev. Lett. **109**, 115301 (2012).

[26] C. Qu, C. Hamner, M. Gong, C. Zhang, and P. Engels, Observation of Zitterbewegung in a spin-orbit coupled Bose-Einstein condensates, Phys. Rev. A **88**, 021604(R) (2013).

[27] A. J. Olson, S.-J. Wang, R. J. Niffenegger, C.-H. Li, C. Greene, and Y. P. Chen, Tunable Laudan-Zener transitions in a spin-orbit-coupled Bose-Einstein condesate, Phys. Rev. A **90**, 013616 (2014).

[28] P. Wang, Z. Yu, Z. Fu, J. Miao, L. Huang, S. Chai, H. Zhai, and J. Zhang, Spin-Orbit Coupled Degenerate Fermi Gases, Phys. Rev. Lett. **109**, 095301 (2012).

[29] L. W. Cheuk, A. T. Sommer, Z. Hadzibabic, T. Yefsah, W. S. Bakr, and M. W. Zwierlein, Spin-Injection Spectroscopy of a Spin-Orbit Coupled Fermi Gas, Phys. Rev. Lett. **109**, 095302 (2012).

[30] R. A. Williams, M. C. Beeler, L. J. LeBlanc, and I. B. Spielman, Raman-Induced Interactions in a Single-Component Fermi Gas Near an s-Wave Feshbach Resonance, Phys. Rev. Lett. **111**, 095301 (2013).

[31] N. Q. Burdick, Y. Tang, and B. L. Lev, Long-Lived Spin-Orbit-Coupled Degenerate Dipolar Fermi Gas, Phys. Rev. X **6**, 031022 (2016).

[32] B. Song, C. He, S. Zhang, E. Hajiyev, W. Huang, X.-J. Liu, and G.-B. Jo, Spin-orbit-coupled two-electron Fermi gases of ytterbium atoms, Phys. Rev. A **94**, 061604(R) (2016).

[33] L. Huang, Z. Meng, P. Wang, P. Peng, S.-L. Zhang, L. Chen, D. Li, Q. Zhou, and J. Zhang, Experimental realization of a two-dimensional synthetic spin-orbit coupling in ultracold Fermi gases, Nat. Phys. **12**, 540 (2016).

[34] Z. Wu, L. Zhang, W. Sun, X.-T. Xu, B.-Z. Wang, S.-C. Ji, Y. Deng, S. Chen, X.-J. Liu, and J.-W. Pan, Realization of two-dimensional spin-orbit coupling for Bose-Einstein condensates, Science **354**, 83 (2016).

[35] Z. Meng, L. Huang, P. Peng, D. Li, L. Chen, Y. Xu, C. Zhang, P. Wang, and J. Zhang, Experimental Observation of Topological Band Gap Opening in Ultracold Fermi Gases with Two-Dimensional Spin-Orbit Coupling, Phys. Rev. Lett. **117**, 235304 (2016).

[36] Note that the creation and annihilation of Dirac points have been recently observed in cold-atom honeycomb lattices through an indirect Landau-Zenner type of transport measurement [18], where the full band dispersion cannot be probed.

[37] A. Eckardt and E. Anisimovas, High-frequency approximation for periodically driven quantum systems from a Floquet-space perspective, New J. Phys. **17**, 093039 (2015).

[38] M. Bukov, L. D'Alessio, and A. Polkovnikov, Universal high-frequency behavior of periodically driven systems: From dynamical stabilization to floquet engineering, Adv. Phys. **64**, 139 (2015).

[39] N. Goldman and J. Dalibard, Periodically Driven Quantum Systems: Effective Hamiltonians and Engineered Gauge Fields, Phys. Rev. X **4**, 031027 (2014).

[40] D. Xiao, M.-C. Chang, and Q. Niu, Berry phase effects on electronic properties, Rev. Mod. Phys. **82**, 1959 (2010).